

Vortex pinning in Au-irradiated FeSe_{0.4}Te_{0.6} crystals from the static limit to gigahertz frequencies

Original

Vortex pinning in Au-irradiated FeSe_{0.4}Te_{0.6} crystals from the static limit to gigahertz frequencies / Torsello, D.; Galluzzi, A.; Okayasu, S.; Fracasso, M.; Gozzelino, L.; Tamegai, T.; Polichetti, M.; Ghigo, G.. - In: PHYSICAL REVIEW. B. - ISSN 2469-9950. - 109:5(2024). [10.1103/PhysRevB.109.054502]

Availability:

This version is available at: 11583/2985730 since: 2024-02-06T15:55:55Z

Publisher:

APS

Published

DOI:10.1103/PhysRevB.109.054502

Terms of use:

This article is made available under terms and conditions as specified in the corresponding bibliographic description in the repository

Publisher copyright

APS postprint/Author's Accepted Manuscript e postprint versione editoriale/Version of Record

This article appeared in PHYSICAL REVIEW. B, 2024, 109, 5, and may be found at <http://dx.doi.org/10.1103/PhysRevB.109.054502>. Copyright 2024 American Physical Society

(Article begins on next page)

Vortex pinning in Au-irradiated FeSe_{0.4}Te_{0.6} crystals from the static limit to gigahertz frequenciesD. Torsello^{1,2,*}, A. Galluzzi^{3,4}, S. Okayasu⁵, M. Fracasso^{1,2},
L. Gozzelino^{1,2}, T. Tamegai⁶, M. Polichetti^{3,4,†} and G. Ghigo^{1,2}¹*Politecnico di Torino, Department of Applied Science and Technology, Torino 10129, Italy*²*Istituto Nazionale di Fisica Nucleare, Sezione di Torino, Torino 10125, Italy*³*Department of Physics E.R. Caianiello, University of Salerno, Fisciano 84084, Italy*⁴*CNR-SPIN Salerno, Fisciano 84084, Italy*⁵*Advanced Science Research Center, Japan Atomic Energy Agency, Tokai, Ibaraki 319-1195, Japan*⁶*Department of Applied Physics, The University of Tokyo, Bunkyo-ku 113-8656, Tokyo, Japan*

(Received 1 August 2023; accepted 19 January 2024; published 5 February 2024)

Fe(Se,Te) is one of the simplest compounds of iron-based superconductors, but it shows a variety of vortex pinning phenomena both in thin-film and single-crystal forms. These properties are particularly important in light of its potential for applications ranging from the development of coated conductors for high-field magnets to topological quantum computation exploiting the Majorana particles found in the superconducting vortex cores. In this paper, we characterize the pinning properties of FeSe_{0.4}Te_{0.6} single crystals, both pristine and Au-irradiated, with a set of characterization techniques ranging from the static limit to the GHz frequency range by using dc magnetometry, ac susceptibility measurements of both the fundamental and the third harmonic signals, and by microwave coplanar waveguide resonator measurements of London and Campbell penetration depths. We observed signatures of single vortex pinning that can be modeled by a parabolic pinning potential, dissipation caused by flux creep, and a general enhancement of the critical current density after 320 MeV Au ion irradiation.

DOI: [10.1103/PhysRevB.109.054502](https://doi.org/10.1103/PhysRevB.109.054502)**I. INTRODUCTION**

Soon after their discovery [1], iron based superconductors (IBSs) attracted a lot of interest because their characteristics are in between those of low-temperature superconductors and cuprates, promising a great technological potential [2]. They are characterized by relatively high critical temperatures, very high critical fields, low anisotropy, and good mechanical properties, a combination that is very appealing for the production of high-field magnets [3]. Among several families of IBSs, Fe(Se,Te) is one of the most studied compounds due to the absence of poisonous elements in its stoichiometry and its simple chemical and structural nature. For these reasons, the development of Fe(Se,Te) coated conductors has been carried out intensely and yielded promising results in a relatively short time [4–6].

Among the features of Fe(Se,Te) relevant for the development of coated conductors for magnet technology, a particularly interesting one is the rich variety of vortex phenomena and of pinning structures that have been reported [7–12]. Moreover, vortex control through pinning could also be critical for other applications such as topological quantum computation allowed by the Majorana particles reported to be present in the vortex core of this material [13].

In this frame, it is particularly interesting to characterize the pinning properties of Fe(Se,Te) in the widest possible

range of conditions and to evaluate how these properties are modified if additional pinning centers are introduced. Ion irradiation is a useful tool to modify the properties of superconductors because the so-introduced defects do not alter the chemical nature of the material, and act both on the superconducting state via carrier scattering [14] and on vortices, being efficient pinning centers [15]. Several studies, both of a fundamental nature and for pinning optimization, were carried out for this reason on IBSs. In particular, FeSe_{0.4}Te_{0.6} was irradiated in the form of thin films with protons at 190 keV [16] and in the MeV energy range [17–22], and with 6 MeV Au ions [23] and of single crystals with 800 MeV Xe [24], 200 MeV Au [24], and 249 MeV Au ions [25]. The latter case, i.e., the irradiation with swift heavy ions, is the most interesting for introducing strong pinning centers.

In this paper, we characterize the pinning properties of FeSe_{0.4}Te_{0.6} single crystals in the pristine state and after irradiation with 320 MeV Au ions resulting in the formation of discontinuous columnar tracks, with a set of measurement techniques that span from the static limit to the GHz frequency range. This approach allowed us to characterize the pinning strength, the dissipation mechanism, and the critical transport parameters over a wide range of frequencies, temperatures, and magnetic fields, yielding a comprehensive view of vortex motion phenomena in this material and on the effect of additional pinning centers.

The paper is structured as follows: first, all the experimental techniques employed for this paper are presented in Sec. II, then the results are presented and discussed in Sec. III, starting from the pinning energy, moving to the dissipation mechanism

*Corresponding author: danielle.torsello@polito.it

†Corresponding author: mpolichetti@unisa.it

before discussing the behavior at high frequencies and finally the resulting critical currents. Lastly, conclusions are drawn and summarized in Sec. IV.

II. EXPERIMENTAL TECHNIQUES AND THEORETICAL METHODS

A. Crystal growth

Single-crystalline samples with nominal composition $\text{FeSe}_{0.4}\text{Te}_{0.6}$ were prepared from high-purity Fe and Se grains and Te powder with stoichiometric quantities that were heated up to 1070 °C for 36 h in vacuum, followed by slow cooling. As-grown crystals were then annealed in 1% oxygen atmosphere at 400 °C for 24 h, followed by quenching. The obtained crystal cleaves perpendicular to the c axis [26], so it was possible to shape the sample as a thin platelet of size $15 \times 200 \times 500 \mu\text{m}^3$. The phase purity and the chemical composition of the crystals were confirmed by powder x-ray diffraction and EDX.

B. Ion irradiation

The 320-MeV Au ion irradiation was performed using a tandem accelerator at the Japan Atomic Energy Agency, Japan, at a fluence of 10^{11} cm^{-2} , with the beam parallel to the crystal c axis. The thickness of the samples was smaller than the implantation range of the 320-MeV Au ions that is about 17 μm . The choice of using single crystals instead of thin films eliminated indirect irradiation effects related to the modification of the substrate that exerts strain on the superconducting films [22]. This kind of irradiation in IBSs produces linearly correlated defects similar to intermittent columnar ones [24]. The cross section of the defects has a diameter of about 3 nm, comparable to the coherence length. Unlike the case of heavy-ion-irradiated cuprates, the amorphous defect core is metallic [25]. Such a structure is expected to provide a strong pinning potential for vortices generated by magnetic fields applied parallel to the c axis of the crystal. The employed fluence corresponds to a matching field of about 2 T. Samples were investigated with all measurement techniques both in the pristine state and after irradiation.

C. dc and ac magnetic susceptibility

The magnetic measurements were carried out by using a 9 Tesla Quantum Design PPMS (Physical Properties Measurement System), provided with an ac measurement system insert which allows performing both dc and ac measurements. Before each measurement, the residual trapped field inside the superconducting magnet was reduced below 1 Oe [27] to prevent any uncontrolled effect on the sample response [28].

For what concerns the dc measurements, the magnetic moment as a function of field $m(H)$ was obtained by means of the dc extraction method. Regarding the ac measurements, the ac magnetic moment as a function of temperature was acquired at different frequencies ($\nu = 107, 1077, 5385$, and 9693 Hz) at fixed ac field amplitude $h_{ac} = 10 \text{ Oe}$, with and without superimposed dc fields ranging from 0 T up to 9 T. For the temperature-dependent ac measurements, the sample was cooled down to 2.5 K in the absence of magnetic field.

Then, the ac and dc fields were switched on and the data were acquired for increasing temperature up to 18 K with a sweep rate of 0.1 K/min. For the dc field dependence of the ac magnetic moment, once the sample reached the target temperature, sufficient time to achieve thermal stabilization was waited. After that, the ac and dc fields were turned on and the data were acquired for increasing dc field up to 9 T with a field increment of 0.05 T. Both the dc and ac measurements were performed by applying the magnetic field parallel to the c axis of the crystal.

D. Coplanar waveguide resonator

Coplanar waveguide resonator (CPWR) measurements in a resonator perturbation approach were successfully used to investigate the London penetration depth, quasiparticle conductivity, and surface impedance of small single crystals of IBSs [29] allowing the investigation of disorder effects [14,30], gap structure [31], anisotropy [32], and magnetic behavior [33,34]. To increase the quality factor of the CPWR and therefore to increase the sensitivity of the method, we operate with a resonator that is superconducting itself, made by patterning an $\text{YBa}_2\text{Cu}_3\text{O}_{7-x}$ (YBCO) thin film. Its operating frequency is at about 8 GHz. By positioning the CPWR with the surface parallel to the magnetic field direction, it is possible to add a dc magnetic field without the problem of screening from the YBCO strip, and therefore study the vortex physics in the crystal. The crystal was placed with the c axis parallel to the magnetic field and to the plane of the central strip of the CPWR ($H \parallel c$ axis of the IBS) with the help of vacuum grease.

By performing a CPWR measurement without applied H_{dc} , one can obtain the London penetration depth $\lambda_L(T)$, the quasiparticle conductivity $\sigma_1(T)$, and the surface resistance $R_s(T)$ and reactance $X_s(T)$, as thoroughly explained in previous works [29,35,36]. The measurement was then repeated at exactly the same conditions, except for the additional presence of H_{dc} . When a magnetic field penetrates the sample in the mixed state, a complex resistivity term given by the presence of vortices (ρ_{vm}) needs to be added to the surface resistance expression that in the local limit reads [37]

$$Z_s = \sqrt{i\mu_0\omega(\rho + \rho_{vm})}, \quad (1)$$

where $\rho = 1/(\sigma_1 - i\sigma_2)$ are the terms describing the superfluid in the absence of vortices [σ_1 is the quasiparticle conductivity, $\sigma_2 = 1/(\mu_0\omega\lambda_L^2)$] and $\rho_{vm} = \rho_{vm,1} + i\rho_{vm,2}$. For T lower than the critical temperature T_c , where the approximation $\sigma_2 \gg \sigma_1$ is valid, one obtains

$$Z_s = \sqrt{-\mu_0^2\omega^2(\lambda_L^2 + \lambda_C^2) + i\mu_0^3\omega^3\lambda_L^4(\sigma_1 + \sigma_c)}, \quad (2)$$

where λ_L is the London penetration depth $\lambda_C = \sqrt{\rho_{vm,2}/(\mu_0\omega)}$ is the Campbell penetration depth, and $\sigma_c = \rho_{vm,1}/(\mu_0^2\omega^2\lambda_L^4)$ represents the dissipative contribution of vortices. The Campbell penetration depth describes the attenuation range of the ac perturbation of the vortex lattice from the sample surface to the interior, and its knowledge gives access to the shielding current density [38].

The data analysis procedure that allows extracting the penetration depth from the shifts in frequency and quality factor

of the resonator is the same as for zero applied field, but in this case yields an effective $\lambda(H, T)$ instead of λ_L and an effective σ instead of σ_1 . These quantities include the contributions from vortex penetration and motion. From this data, it is finally possible to obtain λ_C and σ_C (in the bulk limit) as follows:

$$\lambda_C(H, T) = \sqrt{\lambda(H, T)^2 - \lambda_L(0, T)^2 - \frac{R_s(H, T)^2 - R_s(0, T)^2}{\mu_0^2 \omega^2}}, \quad (3)$$

$$\sigma_C(H, T) = \frac{2[R_s(H, T)\lambda(H, T) - R_s(0, T)\lambda_L(0, T)]}{\mu_0^2 \omega^2 \lambda_L(0, T)^4}. \quad (4)$$

The measurement sequence was the following. First, the sample was cooled in zero field and measured without applied H_{dc} in warming mode, then the sample was zero-field cooled down to a fixed $T \ll T_c$, H_{dc} was increased while measuring (evaluation of properties vs H_{dc}), then the sample was measured as a function of temperature while slowly increasing T up to above T_c [evaluation of properties vs T in zero field cooling (ZFC)], finally the measurement was repeated vs increasing T also in field cooling (FC) mode. This procedure was followed to perform measurements on $\text{FeSe}_{0.4}\text{Te}_{0.6}$ single crystals with $H_{dc} \parallel c$ axis, allowing us to discuss the behavior of the Campbell penetration depth as a function of temperature in ZFC and FC modes and as a function of applied field. Moreover, from this data one can estimate the critical current and the depairing current.

III. RESULTS AND DISCUSSION

A. Pinning energy

To evaluate the pinning energy values of the samples and to probe their ac magnetic response, the temperature dependence of the ac magnetic moment m_1 was studied. In particular, the imaginary component of the first harmonic m_1'' was measured as a function of the temperature at a fixed ac amplitude ($h_{ac} = 10$ Oe), for different ac frequencies in the range 100 Hz–10 kHz, and for different superimposed dc fields starting from 0 T up to 9 T. In Fig. 1, the $m_1''(T)$ curves are reported at a fixed ac amplitude (10 Oe) and frequency (1077 Hz) for different H_{dc} fields for both the pristine and the irradiated sample. In both panels, it can be seen how T_c shifts to lower values by increasing the dc field.

Another interesting feature is the widening of the $m_1''(T)$ curves with increasing dc field. It is quite evident that the $m_1''(T)$ curves for the pristine sample are slightly noisier and wider than those for the irradiated sample, especially at high dc fields. Since the imaginary component of the first harmonic is related to the dissipation processes inside the sample given by the vortex motion, the fact that the curves for the irradiated sample are narrower than those of the pristine one indicates an increased pinning efficiency. This is also confirmed by the low dissipation [$m_1''(T) \simeq 0$] at low temperatures in the irradiated sample even at $\mu_0 H_{dc} = 9$ T, differently from what happens for the pristine sample. Another peculiarity related to the pinning strength of the sample is the peak position as a function of the applied dc field. For the pristine sample,

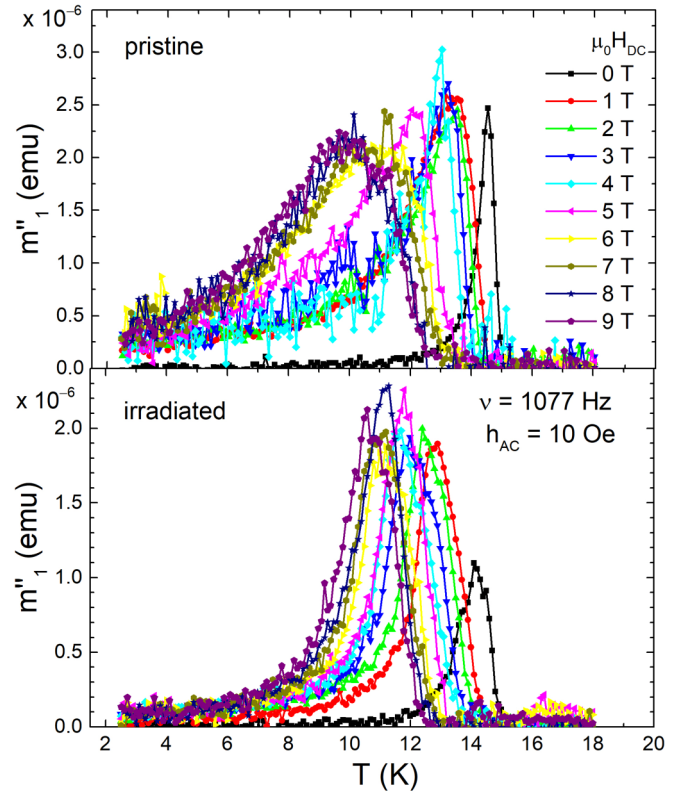


FIG. 1. Temperature dependence of m_1'' at a fixed ac field $h_{ac} = 10$ Oe, fixed frequency $\nu = 1077$ Hz, for dc fields ranging from 0 T up to 9 T for the pristine sample (upper panel) and irradiated sample (lower panel).

$\Delta T_p = T_p^{0T} - T_p^{9T} = 4.8$ K, where T_p^{0T} and T_p^{9T} are the peak temperatures at $\mu_0 H_{dc} = 0$ T and $\mu_0 H_{dc} = 9$ T, respectively. On the other hand, for the irradiated sample, $\Delta T_p = 3.5$ K. The stronger vortex stability of the irradiated sample is also manifested by the smaller temperature shift of the peak temperature over the whole measured field range. By studying the peak temperature T_p of the $m_1''(T)$ curves, it is possible to extract quantitative information on the pinning energy by using the Arrhenius relation [39], which describes the frequency dependence of T_p ,

$$\nu = \nu_0 \exp \frac{-U}{k_B T_p}, \quad (5)$$

where ν_0 is a characteristic frequency, U is the pinning energy, and k_B is the Boltzmann constant.

By plotting $\ln \nu$ vs $1/T_p$ (Arrhenius plots), $\ln \nu_0$ and U/k_B correspond to the intercept and the slope of a straight line, respectively. The Arrhenius plots have been obtained for both pristine and irradiated samples at $h_{ac} = 10$ Oe for different H_{dc} , and fitted with a linear trend. The so-obtained pinning energy values are presented in Fig. 2 as a function of the dc field (at $h_{ac} = 10$ Oe). It is evident that the U values for the irradiated sample are higher than those of the pristine one, confirming also quantitatively what was already reported above. For both $U(H_{dc})$ curves, a decreasing trend for increasing dc fields is visible. This behavior can be described by a power law $U \propto H_{dc}^{(-\alpha)}$, where the exponent α can assume

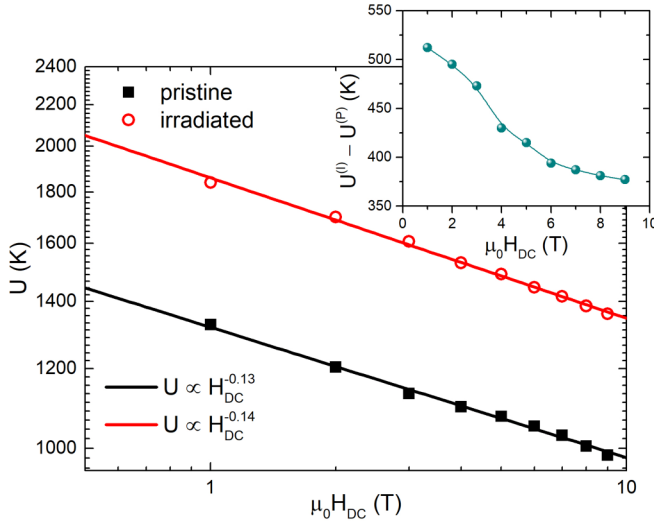


FIG. 2. dc field dependence of the pinning energy U for the pristine sample (black closed square) and irradiated sample (red open circles). The solid lines are the fit of the U data with $U \propto H_{dc}^{(-\alpha)}$. The inset shows the difference between the pinning energy values of the irradiated and pristine samples.

different values depending on the dominant pinning regime acting in the sample. In particular, $\alpha \simeq 0$ corresponds to a single-vortex pinning regime [40], while for $\alpha > 0.5$ collective pinning regime is present [41]. It is interesting to note that $\alpha \simeq 0.13$ – 0.14 (Fig. 2) is almost the same for both samples, denoting a single vortex regime acting in the samples in the whole field range. Therefore, the Au ion irradiation effect on the pristine sample is to enhance the pinning energy values in a range between 510 K at 1 T and 380 K at 9 T (see the inset of Fig. 2), although the vortex pinning regime remains the same.

B. Dissipation mechanism

In Fig. 1, we have shown that the main dissipation processes happen in the temperature interval between 10 K and 13 K for all the applied dc fields used. So, it becomes interesting to study how the dissipation processes of the samples develop in the mentioned temperature range as a function of the dc field. For this reason, m''_1 as a function of the dc field at $T = 10, 11, 12$, and 13 K has been reported in Fig. 3 for $h_{ac} = 10$ Oe and $\nu = 1077$ Hz. The same results were also found at the other frequencies (not reported). It is clear that at $T = 10$ K, the red curve associated with the irradiated sample is always lower than the black one associated with the pristine sample [see Fig. 3(a)]. This means that the sample at 10 K dissipates less after irradiation for all the dc field range. If we increase the temperature, the red curves superimpose over the black ones at certain dc fields [see Figs. 3(b)–3(d)]. Specifically, once the ac field reaches the center of the irradiated sample, the curves overlap, meaning that the dissipation processes are identical in the two samples. It is also worth underlining that the $m''_1(H_{dc})$ values for the irradiated sample at all temperatures increase slower than for the pristine one as the dc field increases. This means that the dissipation processes are less intense in the irradiated sample, and this can indicate a more effective pinning which hinders the vortex

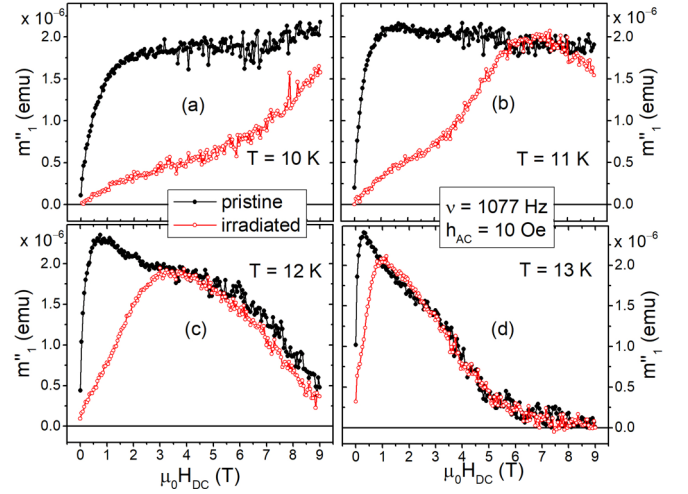


FIG. 3. dc field dependence of m''_1 at a fixed ac field $h_{ac} = 10$ Oe, fixed frequency $\nu = 1077$ Hz, at different temperatures for the pristine sample (black) and irradiated sample (red).

movement in agreement with that reported so far. To have more information about the vortex motion and dynamics, it is possible to study the temperature dependence of the third harmonics of the ac magnetic susceptibility χ [42,43]. Following the approach reported in Ref. [44], the combination of the third and first harmonics (specifically, between χ'_3 and χ''_1), gives direct information on the dissipative regimes acting in the sample [45,46]. It is worth underlining that, in the case of the third harmonics, it is very important to consider all the measurement frequencies since the higher harmonics response is very sensitive to the ac field frequency [47–50] as well as to superimposed dc fields [51–54].

1. ac susceptibility measurements with $H_{dc} = 0$

In Fig. 4, the $\chi'_3(T)$ curves for both the samples are reported for $\nu = 1077$ Hz, $h_{ac} = 10$ Oe, in the absence of dc field (upper panel) and with $H_{dc} = 1$ T (lower panel) together with black and red vertical solid lines individuating the χ''_1 peak temperature (from data shown in Fig. 1) for the pristine and irradiated samples, respectively. This allows us to identify the different dynamical regimes both for $T < T_p(\chi''_1)$ and $T > T_p(\chi''_1)$ by considering the indications obtained by the diffusion equation [49,53,55], together with the results predicted by the Bean critical state model and by using the method reported in Ref. [44]. Specifically, one should have $\chi'_3 = 0$ for $T < T_p(\chi''_1)$ in the Bean critical state model, but clearly this is not verified in the whole temperature range of Fig. 4. This means that in this region the samples are governed by dynamic phenomena which cannot be described in terms of the Bean model. In particular, the dissipation processes can be originated by dynamic regimes such as flux creep, flux flow, thermally activated flux flow (TAFF), and the parallel of flux creep and flow [49]. The TAFF contribution can be neglected because it is relevant only near the onset of the χ'_3 curve [44]. On the contrary, the flux creep, flux flow, and the parallel of flux creep and flow cannot be neglected when the dc field is equal to 0 T. On the other hand, the positive values of χ'_3 and the peak shown for $T > T_p(\chi''_1)$ in the upper panel of

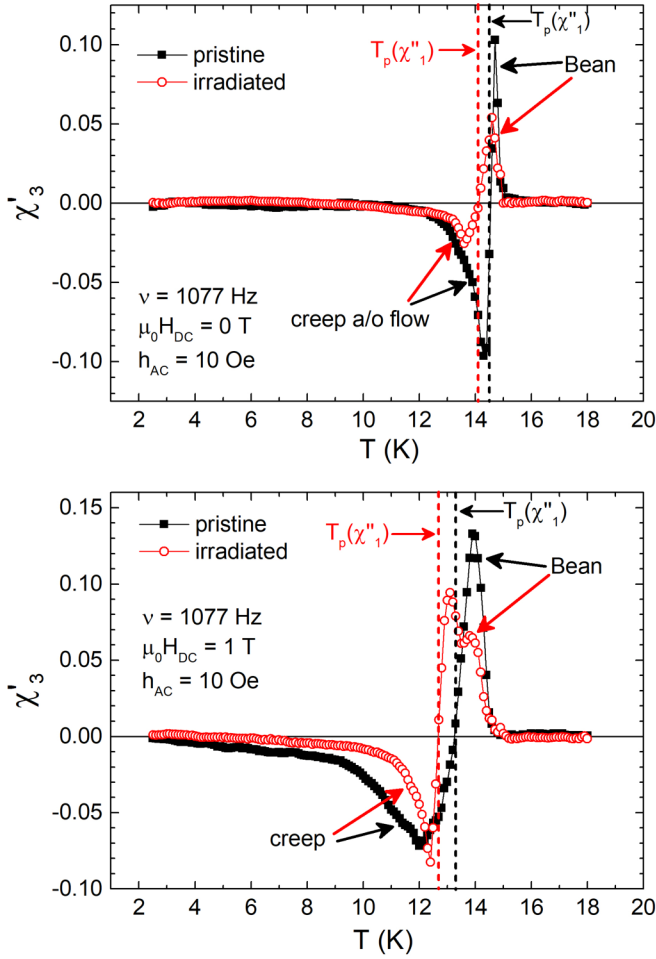


FIG. 4. Temperature dependence of χ'_3 at a fixed ac field $h_{ac} = 10$ Oe, without dc field (upper panel) and with $H_{dc} = 1$ T (lower panel), at a frequency of 1077 Hz for the pristine sample (black closed squares) and irradiated sample (red open circles). The curves were obtained by improving the signal-to-noise ratio.

Fig. 4 for both samples can be explained in the framework of the Bean critical state model. It is interesting to note that at the highest frequencies we investigated ($\nu = 9693$ Hz, not shown), the positive peaks disappear, indicating the absence of the Bean critical state. This could be ascribed to the fact that an increase of the ac frequency corresponds to an increase of the electric field in the superconductor [56], causing intense dissipation processes related to the vortex motion which hinder the critical state formation. This is in agreement with the fact that the negative signal of the curves increases as the frequency increases, indicating an enhancement of the dissipation processes. Moreover, it is interesting to note that for all the ac frequencies, the negative portion of the curves for the pristine sample is always bigger than the respective for the irradiated one. This indicates more intense vortex dynamics associated to the pristine sample, pointing to less efficient pinning.

2. ac susceptibility measurements with $H_{dc} \neq 0$

The same analysis was also performed in presence of a superimposed dc field up to 9 T. Even in the case with $H_{dc} \neq 0$, the information about the flux dynamics can be extracted

analogously by using the combined analysis of the first (T_p position) and third harmonics (real part). However, it is worth underlining that the presence of a dc field much larger than the ac one determines a quasiconstant total field. It has been proved that this causes the disappearance of the flux flow and of the TAFF contribution, generating a linear diffusion process of the magnetic field [49]. This implies that there is no higher harmonic contribution deriving from the flux flow and the TAFF. In the lower panel of Fig. 4, the $\chi'_3(T)$ curves for both samples are reported for the case with a superimposed dc field equal to 1 T. Since $H_{dc} \gg h_{ac}$, the only contribution to the flux dynamics will be represented by the flux creep, which is the only dynamic regime still nonlinear, even in presence of a strong dc field. So, for $T < T_p(\chi''_1)$, both samples show negative values that can be ascribed to flux creep phenomena only, as described in the diffusion equation simulations reported in Refs. [49,53,55]. The measurements performed at different frequencies (not reported) show how these phenomena are stronger as the ac frequency increases due to the increase of the electric field in the superconductor. In this case, the $H_{dc} \neq 0$ T favors the flux creep phenomena because of the lowering of the pinning energy. In this condition, vortices move very fast inside the superconductor flowing similarly to what happens in a flux flow regime. By enhancing the ac frequency value, the third harmonics allow us to individuate the fastest vortices creeping in the superconductor. Moreover, it is interesting to note that the width of the negative portion of the χ'_3 curves is different. In particular, the dynamic phenomena continue for a wider temperature range in the pristine sample for all the frequencies. This indicates that the artificial pins introduced in the sample by irradiation result in a more homogeneous magnetic response together with narrower peaks, confirming the higher pinning efficiency of the irradiated sample. Nevertheless, the vortex dynamics is the same for the two samples being characterized by flux creep phenomena. On the other hand, for $T > T_p(\chi''_1)$, the curves present positive peaks for both samples and at all the ac frequencies, which can be ascribed to the presence of the critical state. Very similar features are visible considering all the dc fields up to 9 T.

C. Campbell penetration depth

As discussed above, for the characterization in the GHz frequency range, the most useful description is in terms of the Campbell penetration depth extracted from the CPWR measurements in the resonator perturbation approach. Figure 5(a) shows the quality factor and resonance frequency shifts given by the presence of a pristine sample coupled to the CPWR without and with an applied dc magnetic field. Clearly, the curves collapse above T_c when vortices are absent. Moreover, the dissipative contribution (related to the quality factor) shows no difference between the ZFC and FC curves.

After the calibration is performed, the penetration depth and complex surface impedance can be obtained and are shown in Figs. 5(b) and 5(c) for the three cases (no applied field, ZFC, and FC). The Campbell penetration depth obtained for ZFC and FC are shown in Fig. 5(d). We find that $\lambda_C(\text{ZFC})$ is very close but larger than $\lambda_C(\text{FC})$. A similar behavior was predicted by a strong pinning model for relatively high fields

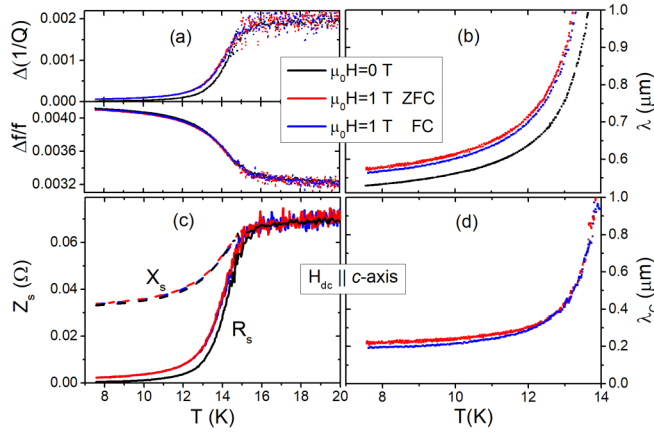


FIG. 5. (a) Quality factor and resonance frequency shifts for the pristine FeSe_{0.4}Te_{0.6} single crystal without applied H_{dc} (black) and with $H_{dc} = 1$ T \parallel c axis in zero-field-cooling (ZFC, red) and field-cooling (FC, blue) modes. (b) Penetration depth and (c) surface impedance curves without applied H_{dc} (black), and with $H_{dc} = 1$ T \parallel c axis in zero-field-cooling (ZFC, red) and field-cooling (FC, blue) modes. (d) Campbell penetration depth curves with $H_{dc} = 1$ T \parallel c axis in ZFC (red) and FC (blue) modes.

[57] and is in agreement with previous observations that were explained by the presence of a macroscopic screening supercurrent which shifts the vortices into a state of inhomogeneous distribution (as in the critical state model) after the ZFC procedure [58]. This displaced vortex lattice is not present when the sample is FC due to the relaxation of the screening currents [59]. The crucial assumption for this explanation is the deviation of the pinning potential from the parabolic shape [58]. Therefore, the small difference in our data suggests that a parabolic description is a good approximation for our samples at the frequencies explored here. From this point on, we always focus on the ZFC data.

The Campbell penetration depth for both the pristine and irradiated samples are shown as a function of temperature and magnetic field in Figs. 6 and 7, respectively. At an applied field of $\mu_0 H_{dc} = 1$ T, the $\lambda_c(T)$ curve of the irradiated sample crosses that of the pristine one at about $T = 11.5$ K. This means that at these high frequencies, the irradiated sample has more efficient pinning at low temperatures (due to the additional pinning centers induced by the irradiation) but at higher temperatures suffers from the overall worsening of the superconducting properties induced by the increased scattering [15]. From Fig. 7, it is evident how the pinning improves with increasing fields in the 0–1 T range.

D. Critical and depairing currents

The dc critical current density $J_{c,dc}$ has been extracted using the Bean critical state model [60,61] from the superconducting hysteresis loops obtained with the dc measurements in the PPMS using

$$J_{c,dc} = \frac{20\Delta M}{[b(1 - \frac{b}{3a})]}, \quad (6)$$

where $\Delta M = M_{dn} - M_{up}$ is the difference between the magnetization measured for decreasing (M_{dn}) and increasing

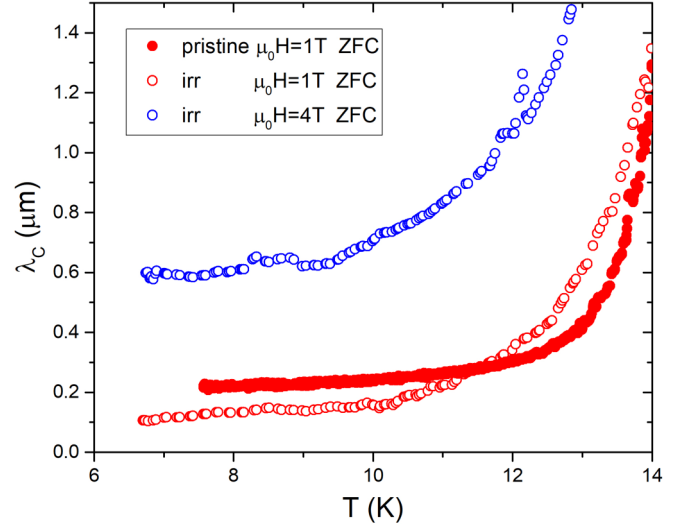


FIG. 6. Campbell penetration depth of pristine and irradiated samples as a function of temperature.

(M_{up}) applied fields, respectively. a and b are the lengths characterizing the cross section of the sample perpendicular to the applied field ($H \parallel c$). The $J_{c,dc}(H_{dc})$ curves so obtained have been reported in Fig. 8 for the pristine sample (upper panel) and for the irradiated sample (lower panel). It is evident that the $J_{c,dc}(H_{dc})$ curves for the irradiated sample are less noisy than those of the pristine sample. This can (once again) indicate a better pinning efficiency due to the Au ion irradiation. Additionally, the $J_{c,dc}$ values shown for the irradiated sample are larger than for the pristine sample, at least at low fields. To better evaluate this last feature, the comparison of the field dependence of $J_{c,dc}$ for the pristine and irradiated samples at $T = 6$ K is reported in Fig. 9 as a representative example. In the inset, the ratio between the $J_{c,dc}(H_{dc})$ values for the irradiated sample over the pristine one is reported. It turns out that the $J_{c,dc}$ of the irradiated sample is always

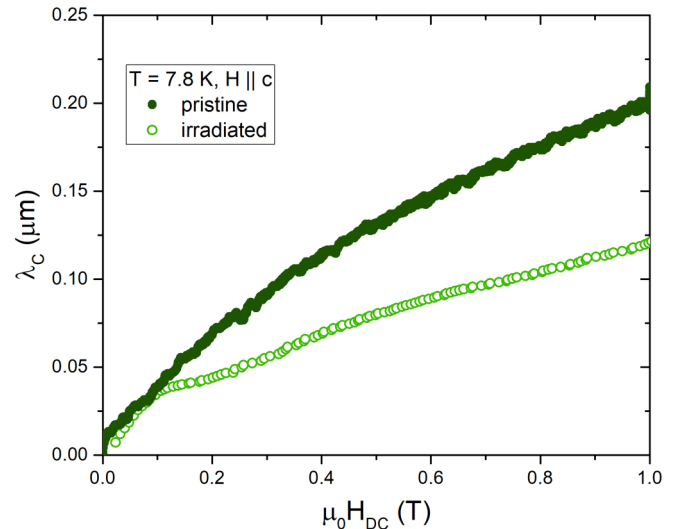


FIG. 7. Campbell penetration depth of the pristine and irradiated samples as a function of the applied magnetic field.

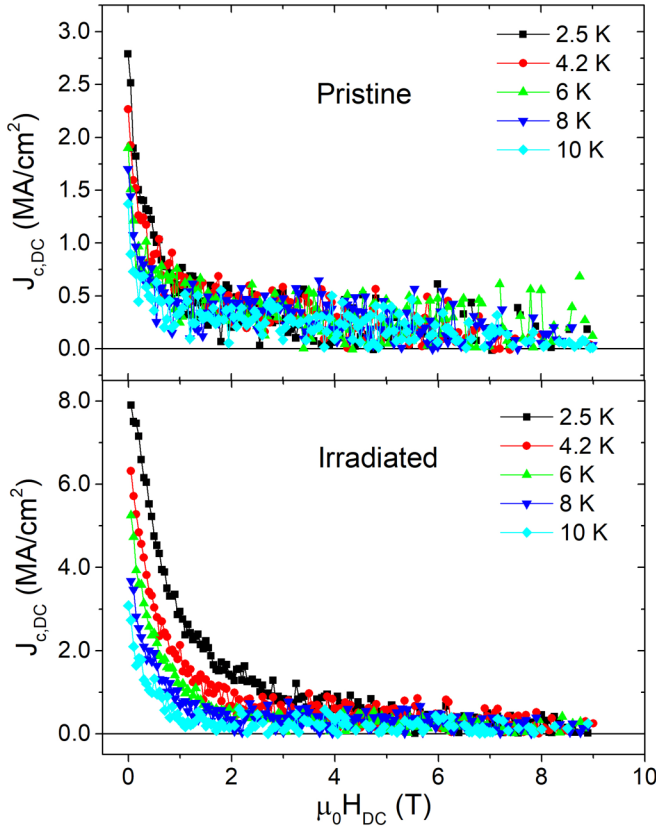


FIG. 8. Critical current density $J_{c,dc}$ as a function of the field at different temperatures for the pristine sample (upper panel) and for the irradiated sample (lower panel).

higher than that of the pristine sample, especially up to fields comparable to the matching field, as shown in the inset of Fig. 9.

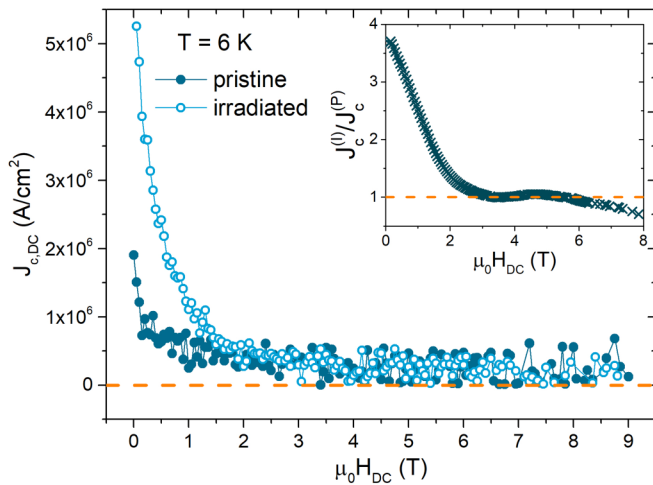


FIG. 9. Critical current density $J_{c,dc}$ as a function of the field at different temperatures for the pristine and irradiated sample at $T = 6$ K (a smoothing procedure was performed). The inset shows the critical current increase due to enhanced pinning, given as the ratio between the irradiated and pristine data.

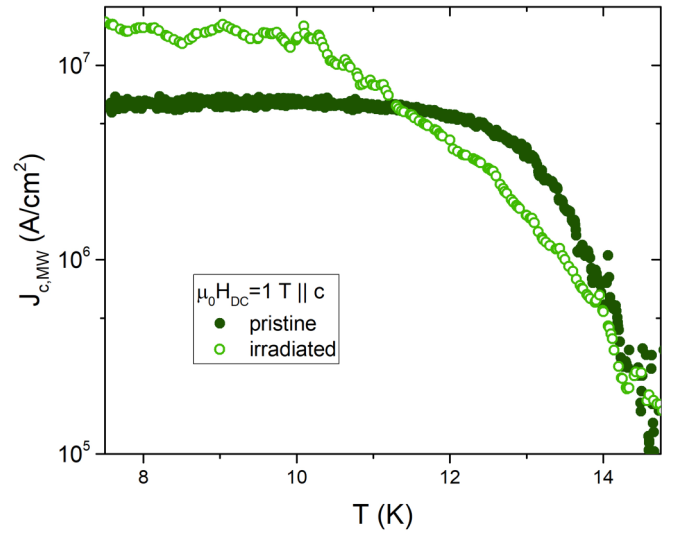


FIG. 10. Critical current densities of pristine and irradiated samples as a function of temperature.

Finally, from the CPWR data set, it is also possible to investigate the critical current density ($J_{c,MW}$) and the depairing current density (J_{dep}). The depairing current density can be expressed, thanks to the Ginzburg-Landau theory, as [62,63]

$$J_{dep} = \Phi_0 / (3^{3/2} \pi \mu_0 \lambda_L^2 \xi), \quad (7)$$

whereas the critical current density can be obtained from the Campbell penetration depth as [38,63,64]

$$J_{c,MW} = H_0 r_p / \lambda_C^2 \simeq H_0 \xi / \lambda_C^2, \quad (8)$$

where the effective radius of the pinning potential, r_p , was substituted by the coherence length, ξ , that can be extrapolated from the $H_{c2}(T)$ data. This expression is valid under the assumption of single vortex pinning and parabolic pinning potential [38,40,65], and is therefore relevant for our case since the parabolic shape of the potential is confirmed by the comparison of ZFC and FC λ_C data, and the single pinning from the susceptibility data. It is important to note that at the high frequency of CPWR measurements, one explores only the bottom of the pinning potential well and flux creep phenomena can reasonably be neglected. Therefore, the critical current obtained by the CPWR measurements should be larger than that measured in the static limit, where the height of the potential well also plays a role.

Figure 10 shows the temperature dependence of the critical current densities obtained from the CPWR data. After irradiation, the critical current increases at low temperatures (better pinning) and decreases closer to T_c (scattering effects), as already discussed from the behavior of λ_C .

The field dependence of the current densities at a temperature of about 8 K is shown in Fig. 11, where dc data is also shown. After irradiation, the depairing current density decreases due to the increase of the London penetration depth and coherence length. The depairing current density is always larger than the critical current, as reasonable. The increase of the critical current density after irradiation is evident from both CPWR and dc data, and the increase ratio is in reasonable agreement as visible from the lower panel. The absolute

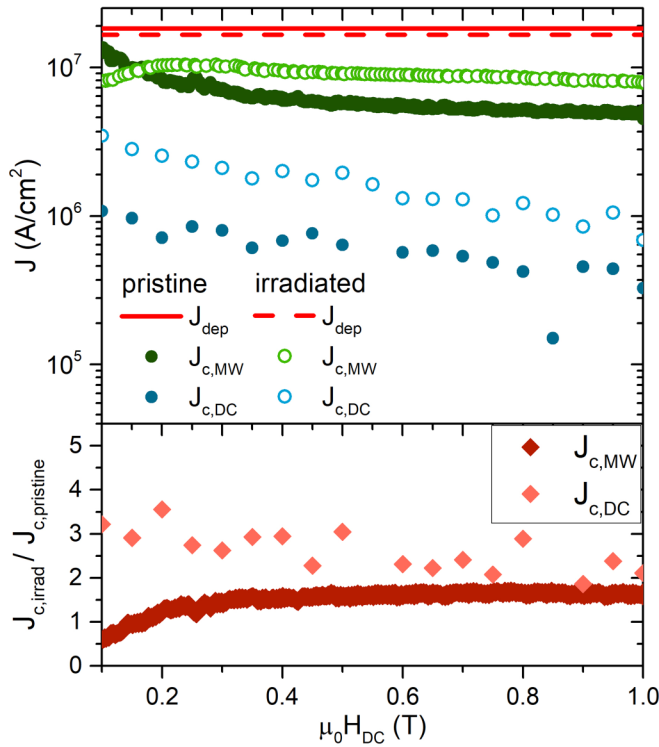


FIG. 11. Upper panel: Critical and depairing current densities of pristine and irradiated samples as a function of applied magnetic field. Lower panel: Relative increase of the critical current densities measured in dc and at high frequency.

values of $J_{c,dc}$ and $J_{c,MW}$ are different because the two measurement techniques do not explore the same phenomena: as mentioned above, with CPWR we explore the bottom of the pinning potential well and its slope (typical vortex displacements in a range < 1 nm), whereas with the magnetometer we explore the potential energy barrier. Therefore, the combination of the two approaches allows for a quite complete description of the pinning potential.

IV. SUMMARIZING REMARKS AND CONCLUSIONS

We reported on the characterization of the vortex pinning behavior in pristine and Au-irradiated $\text{FeSe}_{0.4}\text{Te}_{0.6}$ single

crystals over a frequency range from the static limit up to the microwave regime by employing dc magnetometry, ac susceptibility measurements of both the fundamental and the third harmonic signals, and microwave CPWR measurements. A characterization of pinning over such a broad frequency range (dc to 8 GHz) is a novelty, especially for materials in the single crystal form, that allows us to thoroughly discuss the vortex motion regime and how it is modified by the introduction of defects by heavy ion irradiation. In fact, most of the literature on $\text{Fe}(\text{Se},\text{Te})$ investigates the material grown as thin films [16–23] (where strain effects are often dominant), and little work has been carried out on this material by ac investigation, especially with regard to the harmonics analysis. We found that the vortex interaction can be modeled both in the pristine and irradiated samples by a single vortex pinning potential of parabolic shape, with flux creep occurring above $\simeq T_c/2$ at least up to the kHz range. The introduction of additional correlated defects by 320 MeV Au ion irradiation enhances vortex pinning, especially up to about the matching field, while preserving the qualitative behavior. Since the disordered nature of the $\text{FeSe}_{0.4}\text{Te}_{0.6}$ material provides good pinning centers even in the pristine state ($\alpha = 0.13$), the effect of irradiation with Au ions is to add pinning centers (with different morphology and effectiveness) to a picture in which single vortex pinning is already dominant up to high fields. Overall, this combined experimental approach allows us to achieve a quite comprehensive description of the vortex behavior in small crystalline superconducting samples.

ACKNOWLEDGMENTS

This paper was partially supported by the Ministry of Education, Universities and Research through the PRIN-2017 program, project HIBiSCUS, Grant No. 201785KWLE, and by the European Cooperation in Science and Technology (COST) Action No. CA19108: High-Temperature Superconductivity for Accelerating the Energy Transition D.T. also acknowledges that this study was carried out within the Ministerial Decree No. 1062/2021 and received funding from the FSE REACT-EU - PON Ricerca e Innovazione 2014-2020. This paper reflects only the authors' views and opinions, neither the European Union nor the European Commission can be considered responsible for them.

D.T. and A.G. contributed equally.

- [1] Y. Kamihara, T. Watanabe, M. Hirano, and H. Hosono, *J. Am. Chem. Soc.* **130**, 3296 (2008).
- [2] M. Putti, I. Pallecchi, E. Bellingeri, M. R. Cimberle, M. Tropeano, C. Ferdeghini, A. Palenzona, C. Tarantini, A. Yamamoto, J. Jiang, J. Jaroszynski, F. Kametani, D. Abramov, A. Polyanskii, J. D. Weiss, E. E. Hellstrom, A. Gurevich, D. C. Larbalestier, R. Jin, B. C. Sales *et al.*, *Supercond. Sci. Technol.* **23**, 034003 (2010).
- [3] G. Sylva, E. Bellingeri, C. Bernini, G. Celentano, C. Ferdeghini, A. Leveratto, M. Lisitskiy, A. Malagoli, N. Manca, A. Mancini, P. Manfrinetti, I. Pallecchi, A. Provino, M. Putti, A. Vannozzi, and V. Braccini, *Supercond. Sci. Technol.* **33**, 114002 (2020).
- [4] W. Si, S. J. Han, X. Shi, S. N. Ehrlich, J. Jaroszynski, A. Goyal, and Q. Li, *Nat. Commun.* **4**, 1347 (2013).
- [5] Z. Xu, P. Yuan, Y. Ma, and C. Cai, *Supercond. Sci. Technol.* **30**, 035003 (2017).
- [6] G. Sylva, A. Augieri, A. Mancini, A. Rufoloni, A. Vannozzi, G. Celentano, E. Bellingeri, C. Ferdeghini, M. Putti, and V. Braccini, *Supercond. Sci. Technol.* **32**, 084006 (2019).
- [7] D. Miu, T. Noji, T. Adachi, Y. Koike, and L. Miu, *Supercond. Sci. Technol.* **25**, 115009 (2012).
- [8] T. Tamegai, Y. Sun, T. Yamada, and S. Pyon, *IEEE Trans. Appl. Supercond.* **26**, 1 (2016).

- [9] M. Bonura, E. Giannini, R. Viennois, and C. Senatore, *Phys. Rev. B* **85**, 134532 (2012).
- [10] S. Hossaini, S. Ghorbani, H. Arabi, X. Wang, and C. Lin, *Solid State Commun.* **246**, 29 (2016).
- [11] P. Das, A. D. Thakur, A. K. Yadav, C. V. Tomy, M. R. Lees, G. Balakrishnan, S. Ramakrishnan, and A. K. Grover, *Phys. Rev. B* **84**, 214526 (2011).
- [12] M. Polichetti, A. Galluzzi, K. Buchkov, V. Tomov, E. Nazarova, A. Leo, G. Grimaldi, and S. Pace, *Sci. Rep.* **11**, 7247 (2021).
- [13] T. Machida, Y. Sun, S. Pyon, S. Takeda, Y. Kohsaka, T. Hanaguri, T. Sasagawa, and T. Tamegai, *Nat. Mater.* **18**, 811 (2019).
- [14] D. Torsello, L. Gozzelino, R. Gerbaldo, T. Tamegai, and G. Ghigo, *Sci. Rep.* **11**, 5818 (2021).
- [15] D. Torsello, R. Gerbaldo, L. Gozzelino, F. Laviano, A. Takahashi, A. Park, S. Pyon, A. Ichinose, T. Tamegai, and G. Ghigo, *Supercond. Sci. Technol.* **33**, 094012 (2020).
- [16] T. Ozaki, L. Wu, C. Zhang, J. Jaroszynski, W. Si, J. Zhou, Y. Zhu, and Q. Li, *Nat. Commun.* **7**, 13036 (2016).
- [17] G. Sylva, E. Bellingeri, C. Ferdeghini, A. Martinelli, I. Pallecchi, L. Pellegrino, M. Putti, G. Ghigo, L. Gozzelino, D. Torsello, G. Grimaldi, A. Leo, A. Nigro, and V. Braccini, *Supercond. Sci. Technol.* **31**, 054001 (2018).
- [18] D. Ahmad, W. J. Choi, Y. I. Seo, S. Seo, S. Lee, T. Park, J. Mosqueira, G. Gu, and Y. S. Kwon, *New J. Phys.* **19**, 093004 (2017).
- [19] A. Leo, G. Sylva, V. Braccini, E. Bellingeri, A. Martinelli, I. Pallecchi, C. Ferdeghini, L. Pellegrino, M. Putti, G. Ghigo, L. Gozzelino, D. Torsello, S. Pace, A. Nigro, and G. Grimaldi, *IEEE Trans. Appl. Supercond.* **29**, 1 (2019).
- [20] A. Leo, G. Grimaldi, A. Nigro, G. Ghigo, L. Gozzelino, D. Torsello, V. Braccini, G. Sylva, C. Ferdeghini, and M. Putti, *J. Phys.: Conf. Ser.* **1559**, 012042 (2020).
- [21] T. Ozaki, T. Kashihara, I. Kakeya, and R. Ishigami, *Quantum Beam Sci.* **5**, 18 (2021).
- [22] D. Torsello, M. Fracasso, R. Gerbaldo, G. Ghigo, F. Laviano, A. Napolitano, M. Iebole, M. Cialone, N. Manca, A. Martinelli, L. Piperno, V. Braccini, A. Leo, G. Grimaldi, A. Vannozzi, G. Celentano, M. Putti, and L. Gozzelino, *IEEE Trans. Appl. Supercond.* **32**, 1 (2022).
- [23] T. Ozaki, L. Wu, C. Zhang, W. Si, Q. Jie, and Q. Li, *Supercond. Sci. Technol.* **31**, 024002 (2018).
- [24] T. Tamegai, T. Taen, H. Yagyuda, Y. Tsuchiya, S. Mohan, T. Taniguchi, Y. Nakajima, S. Okayasu, M. Sasase, H. Kitamura, T. Murakami, T. Kambara, and Y. Kanai, *Supercond. Sci. Technol.* **25**, 084008 (2012).
- [25] F. Massee, P. O. Sprau, Y.-L. Wang, J. C. S. Davis, G. Ghigo, G. D. Gu, and W.-K. Kwok, *Sci. Adv.* **1**, e1500033 (2015).
- [26] T. Taen, Y. Tsuchiya, Y. Nakajima, and T. Tamegai, *Phys. Rev. B* **80**, 092502 (2009).
- [27] A. Galluzzi, K. Buchkov, E. Nazarova, V. Tomov, G. Grimaldi, A. Leo, S. Pace, and M. Polichetti, *Eur. Phys. J.: Spec. Top.* **228**, 725 (2019).
- [28] A. Galluzzi, A. Nigro, R. Fittipaldi, A. Guarino, S. Pace, and M. Polichetti, *J. Magn. Magn. Mater.* **475**, 125 (2019).
- [29] G. Ghigo and D. Torsello, *Microwave Analysis of Unconventional Superconductors with Coplanar-Resonator Techniques* (Springer International Publishing, Cham, 2022), pp. 3–29.
- [30] G. Ghigo, D. Torsello, G. A. Ummarino, L. Gozzelino, M. A. Tanatar, R. Prozorov, and P. C. Canfield, *Phys. Rev. Lett.* **121**, 107001 (2018).
- [31] D. Torsello, E. Piatti, G. A. Ummarino, X. Yi, X. Xing, Z. Shi, G. Ghigo, and D. Daghero, *npj Quantum Mater.* **7**, 10 (2022).
- [32] D. Torsello, G. A. Ummarino, J. Bekaert, L. Gozzelino, R. Gerbaldo, M. A. Tanatar, P. C. Canfield, R. Prozorov, and G. Ghigo, *Phys. Rev. Appl.* **13**, 064046 (2020).
- [33] G. Ghigo, D. Torsello, R. Gerbaldo, L. Gozzelino, S. Pyon, I. S. Veshchunov, T. Tamegai, and G.-H. Cao, *Supercond. Sci. Technol.* **33**, 094011 (2020).
- [34] G. Prando, D. Torsello, S. Sanna, M. J. Graf, S. Pyon, T. Tamegai, P. Carretta, and G. Ghigo, *Phys. Rev. B* **105**, 224504 (2022).
- [35] D. Torsello, G. A. Ummarino, L. Gozzelino, T. Tamegai, and G. Ghigo, *Phys. Rev. B* **99**, 134518 (2019).
- [36] G. Ghigo, D. Torsello, L. Gozzelino, T. Tamegai, I. S. Veshchunov, S. Pyon, W. Jiao, G.-H. Cao, S. Y. Grebenchuk, I. A. Golovchanskiy, V. S. Stolyarov, and D. Roditchev, *Phys. Rev. Res.* **1**, 033110 (2019).
- [37] R. E. Collin, *Foundations for Microwave Engineering*, 2nd ed. (McGraw-Hill International Editions, Singapore, 1992).
- [38] H. Kim, M. A. Tanatar, H. Hodovanets, K. Wang, J. Paglione, and R. Prozorov, *Phys. Rev. B* **104**, 014510 (2021).
- [39] M. Nikolo and R. B. Goldfarb, *Phys. Rev. B* **39**, 6615 (1989).
- [40] G. Blatter, M. V. Feigel'man, V. B. Geshkenbein, A. I. Larkin, and V. M. Vinokur, *Rev. Mod. Phys.* **66**, 1125 (1994).
- [41] Y. Yeshurun and A. P. Malozemoff, *Phys. Rev. Lett.* **60**, 2202 (1988).
- [42] T. Ishida and R. B. Goldfarb, *Phys. Rev. B* **41**, 8937 (1990).
- [43] K. Buchkov, A. Galluzzi, D. Mancusi, E. Nazarova, S. Pace, and M. Polichetti, *Phys. Scr.* **94**, 085804 (2019).
- [44] M. Polichetti, M. Adesso, and S. Pace, *Eur. Phys. J. B* **36**, 27 (2003).
- [45] M. Adesso, C. Senatore, M. Polichetti, and S. Pace, *Physica C: Superconductivity* **404**, 289 (2004), Proceedings of the third european conference on vortex matter in superconductors at extreme scales and conditions.
- [46] M. G. Adesso, M. Polichetti, and S. Pace, *Physica C: Superconductivity* **401**, 196 (2004), Proceedings of the international cryogenic materials conference: Topical conference on the voltage-current relation in technical superconductors.
- [47] M. J. Qin and C. K. Ong, *Phys. Rev. B* **61**, 9786 (2000).
- [48] O. Ozogul and A. Aydinuraz, *Supercond. Sci. Technol.* **14**, 184 (2001).
- [49] D. Di Gioacchino, F. Celani, P. Tripodi, A. M. Testa, and S. Pace, *Phys. Rev. B* **59**, 11539 (1999).
- [50] C. Senatore, M. Polichetti, D. Zola, T. D. Matteo, G. Giunchi, and S. Pace, *Supercond. Sci. Technol.* **16**, 183 (2003).
- [51] M. Watahiki, S. I. Yoo, and M. Murakami, *Supercond. Sci. Technol.* **10**, 754 (1997).
- [52] K. Buchkov, M. Polichetti, K. Nenkov, E. Nazarova, D. Mancusi, N. Balchev, D. Kovacheva, A. Zahariev, and S. Pace, *Supercond. Sci. Technol.* **28**, 035009 (2015).
- [53] M. Qin and C. Ong, *Physica C: Superconductivity* **319**, 41 (1999).
- [54] C. Senatore, M. Polichetti, N. Clayton, R. Flükiger, and S. Pace, *Physica C: Superconductivity* **401**, 182 (2004), Proceedings of the international cryogenic materials conference:

- Topical conference on the voltage-current relation in technical superconductors.
- [55] M. J. Qin and X. X. Yao, *Phys. Rev. B* **54**, 7536 (1996).
 - [56] C. J. van der Beek, V. B. Geshkenbein, and V. M. Vinokur, *Phys. Rev. B* **48**, 3393 (1993).
 - [57] R. Willa, V. B. Geshkenbein, and G. Blatter, *Phys. Rev. B* **93**, 064515 (2016).
 - [58] R. Prozorov, R. W. Giannetta, N. Kameda, T. Tamegai, J. A. Schlueter, and P. Fournier, *Phys. Rev. B* **67**, 184501 (2003).
 - [59] R. T. Gordon, N. D. Zhigadlo, S. Weyeneth, S. Katrych, and R. Prozorov, *Phys. Rev. B* **87**, 094520 (2013).
 - [60] C. P. Bean, *Phys. Rev. Lett.* **8**, 250 (1962).
 - [61] C. P. Bean, *Rev. Mod. Phys.* **36**, 31 (1964).
 - [62] R. Arpaia, S. Nawaz, F. Lombardi, and T. Bauch, *IEEE Trans. Appl. Supercond.* **23**, 1101505 (2013).
 - [63] M. Tinkham, *Introduction to Superconductivity* (McGraw-Hill, New York, NY, 2004).
 - [64] J. Bardeen, *Phys. Rev. Lett.* **1**, 399 (1958).
 - [65] E. H. Brandt, *Rep. Prog. Phys.* **58**, 1465 (1995).